

# Luminescent nanothermometry using short-wavelength infrared light

*Ol. A. Savchuk,<sup>1</sup> J. J. Carvajal,<sup>\*1</sup> P. Haro-Gonzalez,<sup>2</sup> M. Aguiló,<sup>1</sup> F. Díaz<sup>1</sup>*

<sup>1</sup>Universitat Rovira i Virgili, Departament de Química Física i Inorgànica, Física i Cristal·lografia de Materials i Nanomaterials (FiCMA-FiCNA) - EMaS, Campus Sescelades, E-43007, Tarragona, Spain.

<sup>2</sup>Fluorescence Imaging Group, Departamento de Física de Materiales, Facultad de Ciencias, Universidad Autonoma de Madrid, 28049 Madrid, Spain.

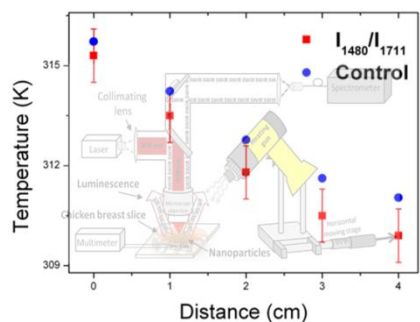
\*corresponding author: [joan josep.carvajal@urv.cat](mailto:joan josep.carvajal@urv.cat)

## **Abstract**

We analyzed the potentiality of the short-wavelength infrared (SWIR) emissions of different lanthanide ions ( $\text{Er}^{3+}$ ,  $\text{Tm}^{3+}$  and  $\text{Ho}^{3+}$ ) embedded in different hosts for luminescence thermometry. The 1.55  $\mu\text{m}$  emission band generated by  $\text{Er}^{3+}$  has different Stark sub-levels that can be used in temperature sensing purposes. However, the thermal sensitivity that can be achieved with this emission is relatively low, ranging from 0.06 to 0.15 %  $\text{K}^{-1}$ . In the case of  $\text{Tm}^{3+}$ , the emissions arising from the  $^3\text{F}_4$  and  $^3\text{H}_4$  electronically coupled energy levels are useful for luminescence thermometry, with a linear evolution for the intensity ratio in the biological range as the temperature increases, which simplifies the calibration procedure for luminescent thermometers based on this parameter. When co-doped with  $\text{Ho}^{3+}$ , an efficient energy transfer

between the  $\text{Tm}^{3+}$  and  $\text{Ho}^{3+}$  ions is generated, that results in a new emission line centered at 1.96  $\mu\text{m}$  that can be also used for luminescence thermometry purposes, with an enhanced thermal sensitivity when pumped at 808 nm. The thermal sensitivities achieved with these doping ions are higher than those obtained with  $\text{Er}^{3+}$  and are comparable to those reported previously for some lanthanide-doped materials operating in the visible, and in the I- and II-BWs. We demonstrated the potentiality of these emissions in the SWIR region for luminescence thermometry and imaging in *ex-vivo* experiments by monitoring the increase of temperature induced in chicken breast meat, with an experimental thermal resolution of  $\sim 0.5$  K, below the theoretical value of 0.8 K predicted for particles operating in this spectral region, and a penetration depth of at least 0.5 cm.

## TOC GRAPHICS



**KEYWORDS:** Luminescence, nanothermometry, SWIR region, nanoparticles, biomedical application.

## 1. INTRODUCTION

Hyperthermia in the treatment of different diseases, like cancer, requires monitoring the body temperature to ensure patient safety,<sup>1,2</sup> and to ensure that heat has been adequately applied to the

affected area, preventing damages in the surrounding health tissue. Moreover, any temperature increment in the body is usually a sign of the presence of a disease or infection.<sup>3</sup> Thus, temperature monitoring techniques are called to play a major role in assuring safe and effective medical treatments.

Noncontact thermometry methods, which provide fast, accurate and non invasive techniques for monitoring the temperature inside the body,<sup>4</sup> are a real alternative to contact thermometers, especially when local temperature measurements are required. Among the different noncontact thermometry techniques, luminescence thermometry, and especially that based on lanthanide ( $\text{Ln}^{3+}$ ) doped materials, offers a high spatial and thermal resolution,<sup>5,6</sup> as well as a reduced or non-existing toxicity, non photobleaching effect, and the possibility of excitation with low cost near IR diode lasers.<sup>7</sup>

$\text{Ln}^{3+}$ -based luminescence nanothermometers using upconversion mechanisms that convert efficiently near IR (NIR) radiation to visible light have been extensively studied.<sup>8-10</sup> However, biological tissues exhibit strong extinction coefficients in the visible, restricting their use for biomedical applications. A reduced absorption and scattering in biological tissues can be achieved by using specific wavelengths lying in the NIR, in the so called biological or therapeutic windows (BWs).<sup>11,12</sup> That allowed demonstrating, for instance, *in-vivo* temperature controlled photothermal therapy of tumors.<sup>13</sup> However, still the quest for a material that maximizes the luminescence quantum efficiency in this region, allowing for high penetration depths in the body is a matter of special interest.<sup>14-21</sup>

Despite all this work, the number of studies exploring the possibilities of longer emission wavelengths in luminescence thermometry are scarce. Naczynski et al.<sup>22</sup> reported that longer wavelengths than those considered in the BWs, lying in the so called short-wavelength IR

(SWIR) that extends from 1.35 to 2.3  $\mu\text{m}$ , transmit more effectively (up to three times) through specific biological tissues (oxygenated blood and melanin-containing tumors), achieving higher penetration depths due to the reduced tissue absorbance and scattering within this region. In fact, in a real scenario in which light penetrates through multiple tissue layers, and in which refractive index changes experienced by light would lead to greater scattering conditions, SWIR light would show higher signal-to-background ratios than visible or NIR light by filtering out biological tissue autofluorescence.<sup>23,24</sup>

Here, we analyze the possibilities for temperature sensing purposes of the emissions in the SWIR region generated by  $\text{Er}^{3+}$ ,  $\text{Tm}^{3+}$  and  $\text{Ho}^{3+}$  ions in different host matrices, including fluorides ( $\text{NaYF}_4$ ), oxyfluorides ( $\text{NaY}_2\text{F}_5\text{O}$ ), simple oxides ( $\text{Lu}_2\text{O}_3$ ) and complex oxides ( $\text{KLu}(\text{WO}_4)_2$ ). The reason we followed to have chosen these materials is their phonon energies, that normally increases from fluorides to complex oxides, and might play a significant role in the non-radiative relaxation processes that can happen in these materials. In fact, fluorides are in general materials with low phonon energies that tend to avoid depopulation processes of the electronic levels due to interaction with phonons.<sup>25-27</sup> From another side, in oxyfluorides and oxides the probabilities of non-radiative relaxations to occur increases. While being detrimental for the maximization of their emitting properties, these processes might be of interest to increase the thermal sensing efficiency or sensitivity for thermometric applications, as we have shown previously.<sup>28,29</sup> The thermometric responses of these particles are compared with those shown by other  $\text{Ln}^{3+}$ -doped nanoparticles operating in the visible, and in the BWs, and demonstrated the potentiality of SWIR emitting nanoparticles for temperature measurements in biological tissues by using chicken breast meat. The results indicate that SWIR emitting nanoparticles are good candidates for luminescent thermometry in biomedical applications.

## 2. EXPERIMENTAL SECTION

**2.1 Nanoparticles used.** Hexagonal 1 % Er, 20 % Yb:NaYF<sub>4</sub>, 1 % Tm, 20 % Yb:NaYF<sub>4</sub> and 1 % Er, 20 % Yb:NaY<sub>2</sub>F<sub>5</sub>O particles were purchased to Boston Applied Technology. As received particles were mixed with water and centrifugated at 8,000 rpm to separate microparticles from nanoparticles. Only particles with nanometer sizes were used in this work.

4 % Er, 20 % Yb doped Lu<sub>2</sub>O<sub>3</sub> nanoparticles were synthesized by the modified Pechini sol-gel method.<sup>30</sup> Lu<sub>2</sub>O<sub>3</sub> (99.9999%), Er<sub>2</sub>O<sub>3</sub> (99.9%) and Yb<sub>2</sub>O<sub>3</sub> (99.9%) were dissolved in hot nitric acid to form the nitrate salts. The nitrate salts were dissolved in an aqueous solution, and ethylenediaminetetraacetic acid (EDTA), used as complexation agent, was added with a molar ratio to metal cations  $CM = [EDTA]/[METAL] = 1$ . After that, ethylene glycol (EG), used as esterification agent, was added to the mixture in a molar ratio  $CE = [EDTA]/[EG] = 2$ , and the solution was heated to 323 K under constant stirring to form a transparent solution. Then, the solution was dehydrated at 363 K to form a polymeric viscous white gel, before it was calcined at 573 K to eliminate the organic compounds and form the precursor powders. Finally, the samples were calcined at 1073 K for 2 h to obtained the nanocrystalline powder.

Monoclinic KLu(WO<sub>4</sub>)<sub>2</sub> singly doped with 1 % Tm; co-doped with 1 % Tm, 10 % Yb; 1 % Tm, 1.5 % Ho or 3 % Er, 10 % Yb, and triply doped with 1 % Tm, 10 % Yb, 1.5 % Ho were synthesized also by the modified Pechini sol-gel method.<sup>21</sup> Monoclinic double tungstate nanoparticles were chosen as an example of a complex oxide because of the excellent results obtained in luminescence thermometry when using these materials in other spectral ranges.<sup>21,31,32</sup> For that, stoichiometric proportions of Ho<sub>2</sub>O<sub>3</sub> (99.9999%), Tm<sub>2</sub>O<sub>3</sub> (99.9%), Yb<sub>2</sub>O<sub>3</sub>, and Lu<sub>2</sub>O<sub>3</sub> were dissolved in hot nitric acid to form the nitrate precursors. In this case we used citric acid

(CA) as the chelating agent, with the same molar ratio, together with ammonium tungstate  $(\text{NH}_4)_2\text{WO}_4$  (99.99%) and potassium carbonate  $\text{K}_2\text{CO}_3$  (99.99%). The aqueous solution was heated at 353 K under magnetic stirring during 24 h until complete dissolution. After adding EG, the solution was heated at 373 K to generate the polymeric gel that was calcined at 1023 K for 2 h to form the desired nanoparticles.

**2.2 Structural and morphological characterization.** The crystalline structure of all nanoparticles was investigated by means of X-ray powder diffraction analysis using a Bruker-AXS D8-Discover diffractometer using  $\text{Cu K}\alpha$  radiation, getting in all cases the crystalline phase desired. Results are summarized in Fig. S1-S3 in the Supporting Information.

The size and morphology of all the samples were investigated by using a transmission electron microscope (TEM) JEOL 1011 operating with an accelerating voltage of 100 kV. The results are also summarized in the Supporting Information (see Fig. S1-S3).

**2.3 Comparative intensity photoluminescence measurements.** Nanoparticles were placed in a borosilicate bottom flat vial and compacted to ensure that they fully fill the bottom of the vial. The vial was inserted in a sample holder that was placed inside an integrating sphere (Labsphere 4GPS-020-SL). Samples were excited with a 200  $\mu\text{m}$  core diameter fiber-coupled laser diode from Apollo Instruments, Inc. emitting at 808 or 980 nm. The laser beam was collimated to a spot size of 3 mm on the sample, and a power of 100 mW. The emission arising from the nanoparticles was collected using a Yokogawa AQ6375 optical spectrum analyzer (OSA) under the same operating conditions to ensure that intensity comparison from the different samples is reliable.

**2.4 Temperature dependent photoluminescence measurements.** For the temperature-dependent photoluminescence experiments, the nanoparticles powders (not compressed) were

introduced into a customized Linkam THMS 600 heating stage, with a boron nitride disk that homogenizes the temperature distribution inside the chamber and along the sample. The heating stage was placed in a homemade microscope setup in which the same diode lasers described before, with emissions at 808 and 980 nm were used to excite the sample, using a 40X microscope objective and a N.A. of 0.6, that produced a laser spot of  $\sim 10 \mu\text{m}$  on the sample. The emission was collected by the same microscope objective, and after passing a dichroic filter for elimination of the excitation wavelength, was sent to the Yokogawa AQ6375 OSA.

### 3. RESULTS AND DISCUSSION

**3.1 Er<sup>3+</sup> emissions in the SWIR.** Er<sup>3+</sup>, Tm<sup>3+</sup> and Ho<sup>3+</sup> ions show several SWIR emission lines that can be used in nanothermometry. Spectra of Er<sup>3+</sup>, Yb<sup>3+</sup> co-doped nanoparticles excited at 980 nm and collected inside the integrating sphere are shown in Figure 1(a). The emission spectra consist of a broad band located at around  $1.55 \mu\text{m}$  with an internal structure due to the emission lines arising from the different Stark sublevels. The mechanism of production of this emission band is the following (see Figure 1(b)): after the absorption of a photon at 980 nm by Yb<sup>3+</sup> the electrons of Yb<sup>3+</sup> are promoted to the excited  $^2F_{5/2}$  energy level. Then, an energy transfer from the excited  $^5F_{5/2}$  energy level of Yb<sup>3+</sup> to Er<sup>3+</sup> ions occurs, populating the  $^4I_{11/2}$  energy level of this ion. After, a multiphonon relaxation from the  $^4I_{11/2}$  to the  $^4I_{13/2}$  energy level allows generating the radiative  $^4I_{13/2} \rightarrow ^4I_{15/2}$  transition, whose emission is centered at  $1.55 \mu\text{m}$ .<sup>20</sup>

As can be seen in Figure 1(a), Er,Yb:NaYF<sub>4</sub> nanoparticles show the most intense emission among the materials analyzed. This material already received an important attention for bioimaging applications and nanothermometry in the visible region because

of its efficient upconversion emissions.<sup>9,33,34</sup> Such exception emitting properties seems to be related to their low phonon energies and the short interdopant distance in these compounds.<sup>25-27</sup> Er,Yb:NaY<sub>2</sub>F<sub>5</sub>O and Er,Yb:KLu(WO<sub>4</sub>)<sub>2</sub> nanoparticles show emissions with a similar intensity. Finally, with less intensity, we encounter the Er,Yb:Lu<sub>2</sub>O<sub>3</sub> nanoparticles. Thus, according to these results, fluorides, and in particular NaYF<sub>4</sub>, are the most efficient materials to generate emissions from Er<sup>3+</sup> in the SWIR region after energy transfer from Yb<sup>3+</sup>.

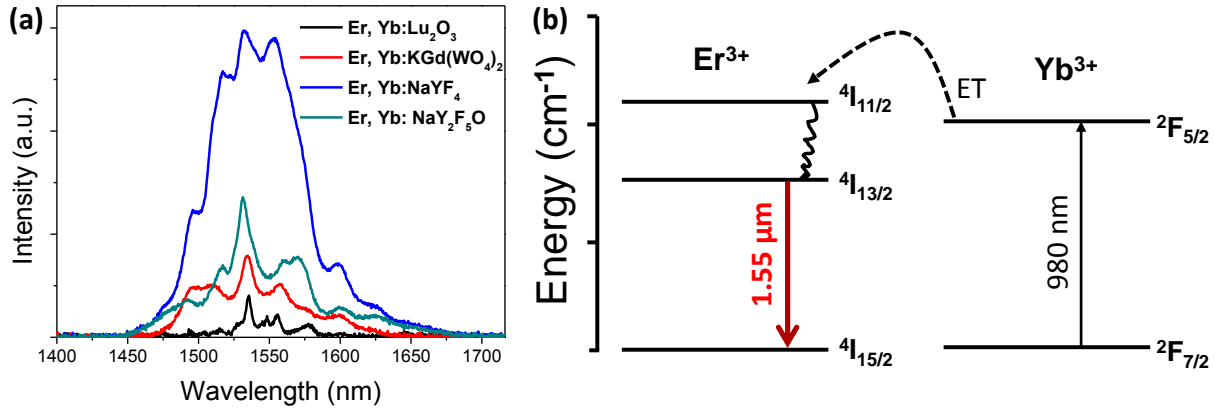


**Figure 1.** (a) Comparison of the intensities obtained for the different hosts co-doped with Er<sup>3+</sup> and Yb<sup>3+</sup> ions after excitation at 980 nm. (b) Mechanism of generation of SWIR emission lines for the nanoparticles codoped with Er<sup>3+</sup> and Yb<sup>3+</sup>.

We analyzed the changes induced by temperature in the intensity of the different emission lines of the band centered at 1.55 μm. The results are presented in Figure 2(a). In general, we observed that when the temperature increases, the intensity of the emission band tends to decrease, especially for these emission lines located at lower energies, while those located at higher energies become less affected. This is due to the different

electronic population of the different Stark sublevels involved in these spectroscopic transitions, indicating, as expected, that they are thermally coupled, and thus, that a fluorescence intensity ratio (FIR) can be defined as a function of temperature as:<sup>35</sup>

$$FIR = \frac{I_1}{I_2} = B \exp\left(-\frac{\Delta E}{k_B T}\right) \quad (1)$$

where  $k_B$  is the Boltzmann constant,  $T$  is the absolute temperature, and  $\Delta E$  is the energy difference between the two Stark sublevels considered. The results are summarized in Figure 2(b).

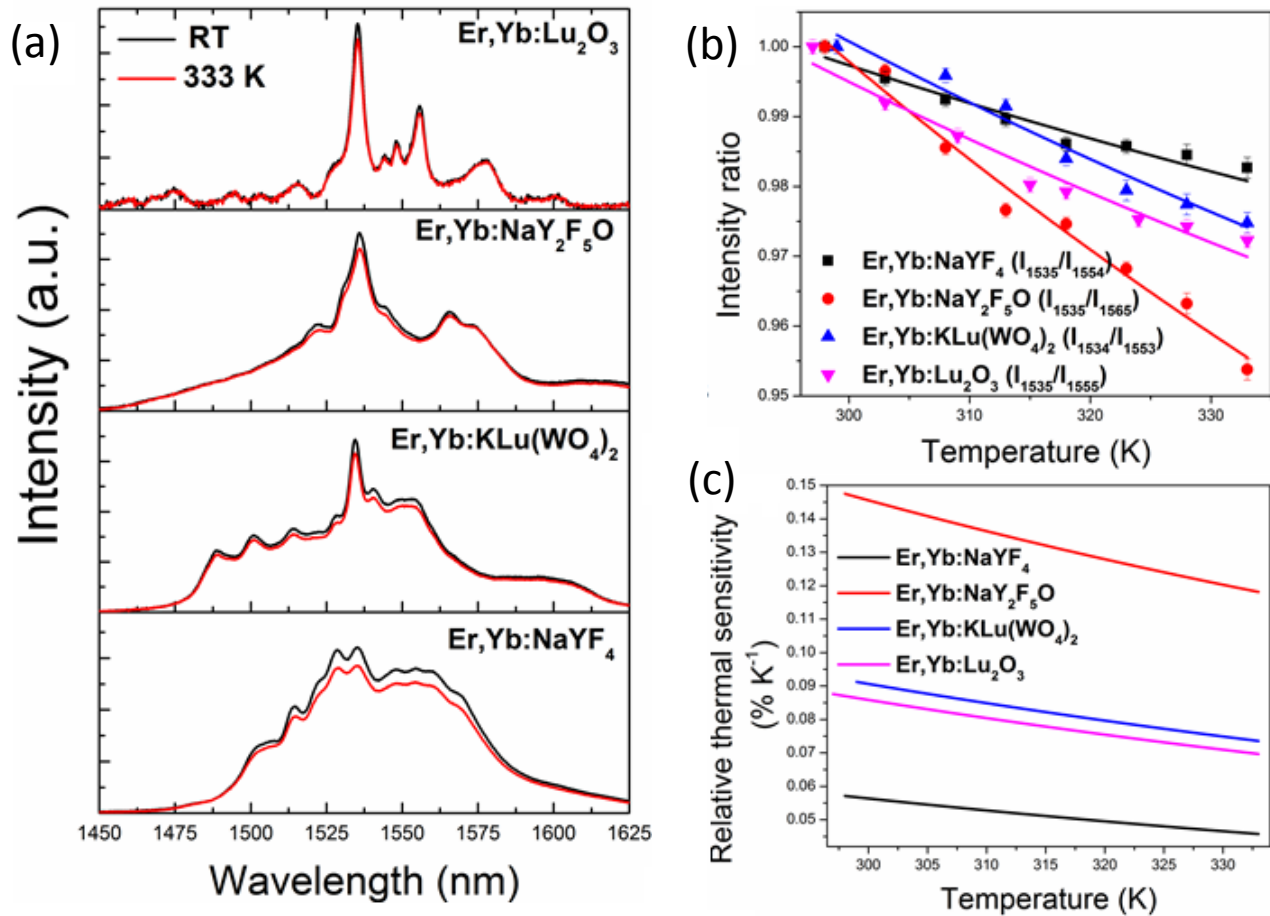


**Figure 2.** (a) 1.55  $\mu\text{m}$  emission of  $\text{Er}^{3+}$ ,  $\text{Yb}^{3+}$  co-doped nanoparticles recorded at room temperature and 333 K. (b) FIR of the emission lines located at 1.535 and 1.555  $\mu\text{m}$  for the different particles as a function of temperature. (c) Relative thermal sensitivity obtained from the FIR for the different samples.

In each case we considered the emission lines that show the highest slope for FIR that coincide with these appearing at  $\sim 1.545$  and  $\sim 1.555$   $\mu\text{m}$ , with the exception of the  $\text{Er,Yb:NaY}_2\text{F}_5\text{O}$  nanoparticles, for which the emission line at  $\sim 1.565$   $\mu\text{m}$  had to be used. The FIR follows an almost linear tendency in all cases and can be fitted to the Boltzmann distribution described in equation 1.<sup>35</sup> The highest FIR slope was observed for  $\text{Er,Yb:NaY}_2\text{F}_5\text{O}$  nanoparticles. The two oxides considered in this work showed almost the same slope (the FIR lines are almost parallel), while the fluoride nanoparticles show the smallest slope. This is a consequence of the activation of phonon-assisted processes and multi-phonon decays caused by temperature increase when oxygen is incorporated in the nanoparticles.<sup>28,29</sup>

Another important parameter to compare the performance of the different luminescent thermometers is the thermal sensitivity, that considers the maximum change of the FIR for each temperature degree. Here, we used the relative thermal sensitivity, which was calculated using the following equation:<sup>5</sup>

$$S_{rel} = \frac{\left(\frac{\partial R}{\partial T}\right)}{R} \quad (2)$$

where  $R$  is the luminescent parameter that changes with temperature (FIR in the present case). The relative thermal sensitivities for the  $\text{Er}^{3+}$  emissions in the SWIR considered in this article are presented in Figure 2(c).  $\text{Er,Yb:NaY}_2\text{F}_5\text{O}$  nanoparticles show the highest

relative sensitivity (0.15 % K<sup>-1</sup>), almost 3 times higher than that of Er,Yb:NaYF<sub>4</sub> nanoparticles.

Despite the relative thermal sensitivities of Er<sup>3+</sup>, Yb<sup>3+</sup> co-doped systems operating in the visible are higher than those analyzed here, it is important to note that the 1.55 μm emission band might be used to monitor temperature changes in telecommunication's systems to prevent optical damages.<sup>36,37</sup>

**3.2 Tm<sup>3+</sup> and Ho<sup>3+</sup> emissions in the SWIR after pumping at 980 nm.** The photoluminescence spectra in the SWIR region of different nanoparticles co-doped with Tm<sup>3+</sup> and Yb<sup>3+</sup> ions excited at a 980 nm are shown in Figure 3(a). The spectra consist of two emission bands located at ~1.45 μm and ~1.8 μm. The mechanism for the generation of these emission lines starts when Yb<sup>3+</sup> absorbs a photon at 980 nm and promotes its electrons to the <sup>2</sup>F<sub>5/2</sub> excited state. Then, an energy transfer process occurs due to the energy match between the Yb<sup>3+</sup> <sup>2</sup>F<sub>5/2</sub> and Tm<sup>3+</sup> <sup>3</sup>H<sub>5</sub> levels. From the <sup>3</sup>H<sub>5</sub> energy level, electrons can relax non-radiatively to the <sup>3</sup>F<sub>4</sub> level. From here, the energy of a second excited electron of Yb<sup>3+</sup> is transferred to Tm<sup>3+</sup> while its electrons are in the <sup>3</sup>F<sub>4</sub> excited state, promoting them to the <sup>3</sup>F<sub>3</sub> state. Then, a second non-radiative relaxation takes place towards the <sup>3</sup>H<sub>4</sub> energy level, from which the emission band located at ~1.45 μm arises, resulting from the <sup>3</sup>H<sub>4</sub> → <sup>3</sup>F<sub>4</sub> transition. When the electrons in the <sup>3</sup>F<sub>4</sub> state relax radiatively to the <sup>3</sup>H<sub>6</sub> ground state, the second emission line, located at 1.8 μm, is generated (see Figure 3(b)).

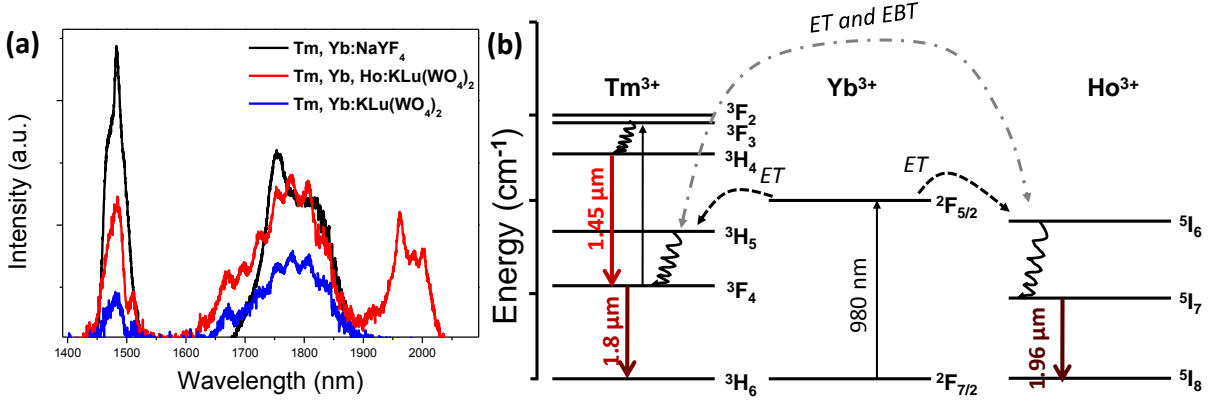


**Figure 3.** (a) Comparison of the emission intensity of the different hosts co-doped with Tm<sup>3+</sup>, Yb<sup>3+</sup> and Ho<sup>3+</sup> ions excited at 980 nm. (b) Mechanisms of generation for the SWIR emission lines for the samples co-doped with Tm<sup>3+</sup>, Yb<sup>3+</sup> and Ho<sup>3+</sup> ions.

When the nanoparticles include also Ho<sup>3+</sup>, an additional line can be observed at 1.96 μm, assigned to the <sup>5</sup>I<sub>7</sub>→<sup>5</sup>I<sub>8</sub> transition of Ho<sup>3+</sup>. This emission can be generated by the energy transfer from Yb<sup>3+</sup> to Ho<sup>3+</sup>. After Yb<sup>3+</sup> absorbed a photon at 980 nm and promoted its electrons to the <sup>2</sup>F<sub>5/2</sub> excited state, it can transfer this energy to the resonant <sup>5</sup>I<sub>6</sub> level of Ho<sup>3+</sup>. From here, and after a non-radiative relaxation towards the <sup>5</sup>I<sub>7</sub> level, a radiative transition to the ground state of Ho<sup>3+</sup> takes place at 1.96 μm.<sup>38</sup> Another possibility for the generation of this emission is a direct energy transfer process from the <sup>3</sup>H<sub>5</sub> level of Tm<sup>3+</sup> to the resonant <sup>5</sup>I<sub>6</sub> level of Ho<sup>3+</sup>, followed by the non-radiative relaxation towards the <sup>5</sup>I<sub>7</sub> level, from which the <sup>5</sup>I<sub>7</sub>→<sup>5</sup>I<sub>8</sub> transition takes place.<sup>39</sup> However, since the concentration of Yb<sup>3+</sup> in the nanoparticles is ten times higher than that of Tm<sup>3+</sup>, the first mechanism seems to be the more plausible.

The highest intensity is observed again for the Tm,Yb:NaYF<sub>4</sub> nanoparticles, followed by the Tm,Yb,Ho:KLu(WO<sub>4</sub>)<sub>2</sub> nanoparticles, with a similar intensity at ~1.8 μm, and with the additional emission band at ~1.96 μm. Tm,Yb:KLu(WO<sub>4</sub>)<sub>2</sub> nanoparticles show the

smallest intensity, in this case, as can be seen in Figure 3(a). So then, the incorporation of  $\text{Ho}^{3+}$  in this material seems to play an important role in transferring additional energy towards  $\text{Tm}^{3+}$  ions through the  $^5\text{I}_6$  and  $^3\text{H}_5$  levels of  $\text{Ho}^{3+}$  and  $\text{Tm}^{3+}$ , respectively, apart from that already transferred from  $\text{Yb}^{3+}$ . Thus, this constitutes a beneficial mechanism to enhance the emission in the SWIR of  $\text{Tm}^{3+}$ .

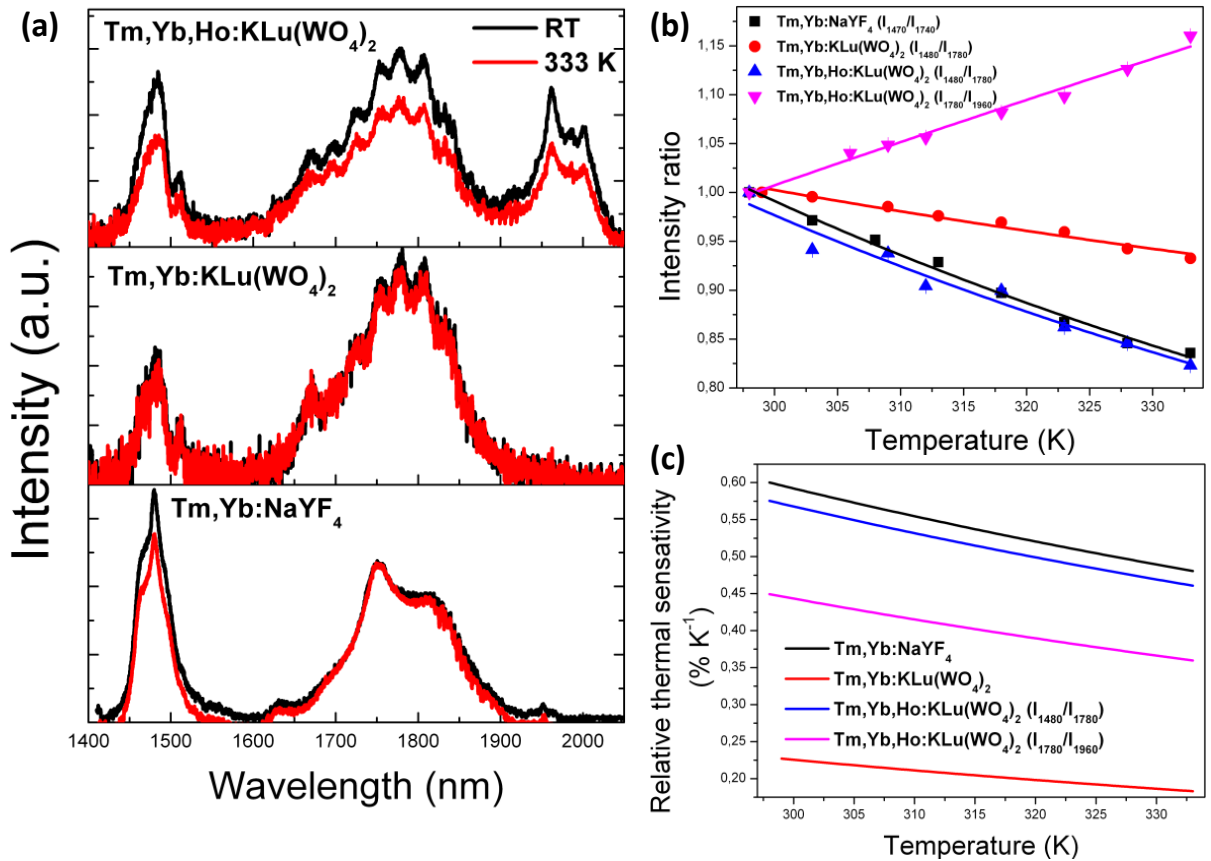


**Figure 4.** (a) SWIR emission of  $\text{Tm}^{3+}$ ,  $\text{Yb}^{3+}$  co-doped and  $\text{Tm}^{3+}$ ,  $\text{Yb}^{3+}$ ,  $\text{Ho}^{3+}$  triply doped samples recorded at room temperature and 333 K. (b) Intensity ratio of the emission lines located at (1470~1480) nm and (1770~1780) nm as a function of temperature for the different nanoparticles analyzed. (c) Relative thermal sensitivity calculated for the  $\text{Tm}^{3+}$ ,  $\text{Yb}^{3+}$  co-doped and  $\text{Tm}^{3+}$ ,  $\text{Yb}^{3+}$ ,  $\text{Ho}^{3+}$  triply doped nanoparticles.

We also analyzed the evolution of the intensity with the temperature of the spectra of  $\text{Tm}^{3+}$ ,  $\text{Yb}^{3+}$  co-doped and  $\text{Tm}^{3+}$ ,  $\text{Yb}^{3+}$ ,  $\text{Ho}^{3+}$  triply doped nanoparticles. Figure 4(a) presents the emission spectra of  $\text{Tm,Yb:NaYF}_4$ ,  $\text{Tm,Yb:KLu(WO}_4)_2$ ,  $\text{Tm,Yb,Ho:KLu(WO}_4)_2$  nanoparticles at room temperature and at 333 K. As can be seen, at high temperatures the emission intensity decreases in all samples. However, the intensity of the emission bands centered at 1.45 and 1.8  $\mu\text{m}$  decreased at different rates as the temperature increased. In fact, the intensity of the 1.45  $\mu\text{m}$  emission is decreasing faster as the temperature increases than that of the 1.8  $\mu\text{m}$  emission. This different behavior in the evolution of the intensities of these two bands with temperature is due to the electronic mechanisms involved in their generation. The 1.8  $\mu\text{m}$  emission is generated from the transfer of the energy of a photon at 980 nm from the  $^2\text{F}_{5/2}$  energy level of  $\text{Yb}^{3+}$  to the resonant  $^3\text{H}_5$  energy level of  $\text{Tm}^{3+}$ , followed by a fast non-radiative relaxation towards the  $^3\text{F}_4$  lower energy level of  $\text{Tm}^{3+}$ , and the radiative relaxation to the  $^3\text{H}_6$  level of  $\text{Tm}^{3+}$ . Instead, to produce the 1.4  $\mu\text{m}$  emission, a second energy transfer process from  $\text{Yb}^{3+}$  when the electron is still in the  $^3\text{F}_4$  excited electronic state, is required. As the temperature increases, this second energy transfer process is less favorable when compared to the mechanism of generation of the 1.8  $\mu\text{m}$  emission. Thus, the electronic population of the  $^3\text{H}_4$  level (via the excited state absorption between the  $^3\text{F}_4$  and the  $^3\text{F}_{2,3}$  levels followed by the non-radiative relaxation to that level) will decrease as the temperature increases, being the cause for the decrease of the intensity of the 1.4  $\mu\text{m}$  emission at a faster rate. This behavior has been already reported before, although for applications in telecommunications to develop an S-band amplifier operating at low temperatures.<sup>40</sup> So, since the  $^3\text{F}_4$  energy level of  $\text{Tm}^{3+}$  is populated by the radiative

relaxation that generates the 1.4  $\mu\text{m}$  emission from the  $^3\text{H}_4$  level, and taking also into account that the same  $^3\text{F}_4$  energy level is the origin of the 1.8  $\mu\text{m}$  emission, we can consider that these two emission lines are somehow electronically linked.<sup>41</sup> Thus, although we cannot consider that these systems are in thermal equilibrium, governed by a Boltzmann distribution, we can observe how the intensity ratio between these two emission bands evolves with temperature, and use it to determine the temperature by luminescence means.<sup>42</sup> Figure 4(b) shows the evolution of the intensity ratio between some selected peaks of these nanoparticles, calculated by deconvoluting the peaks that can be distinguished in the different emission bands, and using the areas determined under each peak. As can be seen the intensity ratio between the emission lines located at 1780 and 1960 nm of Tm,Yb,Ho:KLu(WO<sub>4</sub>)<sub>2</sub> nanoparticles increases as the temperature increases. This is due to the energy transfer and back-transfer processes which are strongly temperature dependent and thus affect the emission intensities of the Tm<sup>3+</sup> and Ho<sup>3+</sup> transitions.<sup>43</sup> This process is dependent, of course, of the distance between Ho<sup>3+</sup> and Tm<sup>3+</sup> in the crystalline structure, which at its turn depends on the concentration of these ions in the nanoparticles. We kept the concentration of Ho<sup>3+</sup> and Tm<sup>3+</sup> ions to concentration levels for which an enhancement of the Tm<sup>3+</sup> emissions in the SWIR were observed. Further increases of the Ho<sup>3+</sup> concentration in Tm,Yb,Ho:KLu(WO<sub>4</sub>)<sub>2</sub> nanoparticles would represent a decrease of the Tm<sup>3+</sup> emissions.<sup>31</sup> The rest of the intensity ratios considered, involving peaks in the 1.45 and 1.8  $\mu\text{m}$  bands decreases as the temperature increases. Among these, the slope of the intensity ratio for Tm,Yb:NaYF<sub>4</sub> and Tm,Yb,Ho:KLu(WO<sub>4</sub>)<sub>2</sub> nanoparticles are almost identical, while that corresponding to the Tm,Yb:KLu(WO<sub>4</sub>)<sub>2</sub> nanoparticles is the smallest among the materials considered.

To compare the performance of these nanoparticles with other luminescent ratiometric nanothermometers we calculated their relative thermal sensitivity using eq. 2. The results are shown in Figure 4(c). Tm,Yb:NaYF<sub>4</sub> and Tm,Yb,Ho:KLu(WO<sub>4</sub>)<sub>2</sub> nanoparticles show the highest relative sensitivity, with a maximum of about 0.6 % K<sup>-1</sup> at room temperature. This thermal sensitivity is higher than that of Er<sup>3+</sup>-doped systems operating in this spectral region. When compared to the thermal sensitivity of other Tm<sup>3+</sup>-doped systems, it is higher than that reported for Tm,Yb:Y<sub>2</sub>O<sub>3</sub> phosphors operating in the visible (0.34 % K<sup>-1</sup>)<sup>44</sup> and higher than that of Tm,Yb:CaF<sub>2</sub> nanoparticles (~0.16 % K<sup>-1</sup>, estimated from the data provided in the publication),<sup>45</sup> Tm,Yb co-doped oxyfluoride glass ceramics (0.3 % K<sup>-1</sup>)<sup>46</sup> and Tm,Yb:LiNbO<sub>3</sub> single crystal (0.024 % K<sup>-1</sup>)<sup>47</sup> operating in the BWs.

**3.3 Tm<sup>3+</sup> and Ho<sup>3+</sup> emissions in the SWIR after pumping at 808 nm.** Tm<sup>3+</sup> can also be excited at 808 nm which allows exploring new possibilities to develop luminescent nanothermometers in the SWIR. The luminescence spectra in the SWIR for Tm-doped, Tm, Yb and Tm, Ho co-doped KLu(WO<sub>4</sub>)<sub>2</sub> nanoparticles are presented in Figure 5. In the case of Tm-doped and Tm, Yb co-doped nanoparticles, the spectra consist of two broad bands centered at 1.45 and 1.8 μm, as expected. Pumping at 808 nm excites electrons from the fundamental <sup>3</sup>H<sub>6</sub> to the excited <sup>3</sup>H<sub>4</sub> energy level of Tm<sup>3+</sup>, from which they decay radiatively to the <sup>3</sup>F<sub>4</sub> level, generating the emission at 1.45 μm, followed by the <sup>3</sup>F<sub>4</sub> → <sup>3</sup>H<sub>6</sub> transition that generates the emission at 1.8 μm, as is depicted in Figure 5(b).

In the case of Tm,Ho:KLu(WO<sub>4</sub>)<sub>2</sub> nanoparticles, an energy transfer process between Tm<sup>3+</sup> and Ho<sup>3+</sup> is produced, as explained before, that generates the additional emission band at 1.96 μm.

The emission intensity for the Tm:KLu(WO<sub>4</sub>)<sub>2</sub> nanoparticles is higher than that obtained for the Tm, Ho co-doped KLu(WO<sub>4</sub>)<sub>2</sub> and Tm,Yb:KLu(WO<sub>4</sub>)<sub>2</sub> nanoparticles. In the case of Tm, Yb co-doped nanoparticles, we also observed the ~1 μm emission corresponding to Yb<sup>3+</sup> (see Figure 5(c)). This can be explained by the energy transfer process from the <sup>3</sup>H<sub>4</sub> excited state of Tm<sup>3+</sup> to the <sup>2</sup>F<sub>5/2</sub> excited state of Yb<sup>3+</sup>, from where it can relax radiatively emitting at ~1 μm through the <sup>2</sup>F<sub>5/2</sub> → <sup>2</sup>F<sub>7/2</sub> transition, as it is described in Figure 5(b). This energy transfer process between Tm<sup>3+</sup> and Yb<sup>3+</sup>, that seems to be very efficient, would be the responsible for the reduced intensity of the Tm<sup>3+</sup> emissions in Tm,Yb:KLu(WO<sub>4</sub>)<sub>2</sub> nanoparticles. The reduced intensity for the Tm,Ho:KLu(WO<sub>4</sub>)<sub>2</sub> nanoparticles compared to that of Tm:KLu(WO<sub>4</sub>)<sub>2</sub> nanoparticles would be explained by the energy transfer between Tm<sup>3+</sup> and Ho<sup>3+</sup>. As mentioned before, this process depends on the distance among doping ions in the crystalline structure, which can be tuned by their concentration. We kept the concentration of Ho<sup>3+</sup> and Tm<sup>3+</sup> at levels for which the heating effect generated by the particles after pumping at 808 nm is minimum in order not to affect their potential applications as thermometers.

We, then, analyzed the possibilities of using the emissions generated by Tm-doped nanoparticles pumped at 808 nm as luminescent thermometers. The evolution of the intensity of the SWIR emissions arising from these nanoparticles when the temperature increases is presented in Figure 6(a). Again, we observe that the evolution of the intensity of the different emission bands is different as the temperature increases.

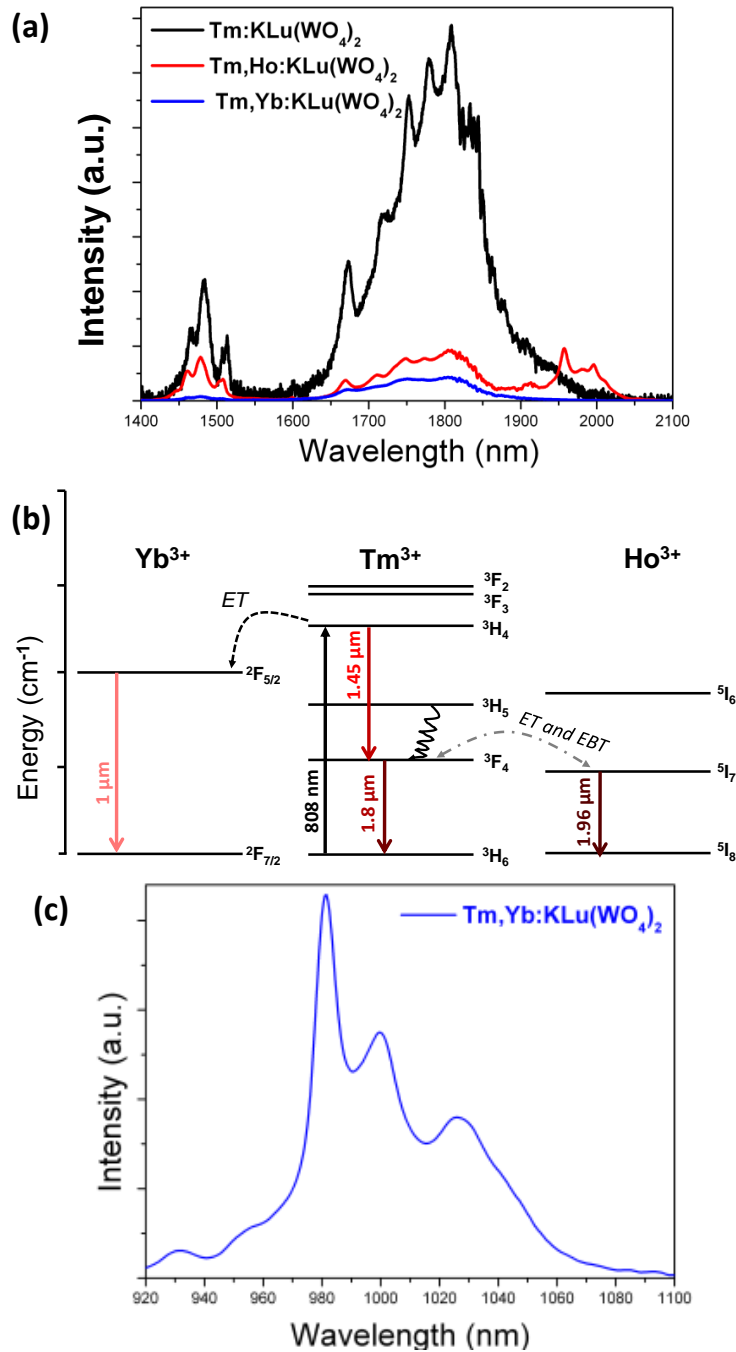


**Figure 5.** (a) Comparison of the emission intensity in the SWIR region of KLu(WO<sub>4</sub>)<sub>2</sub> nanoparticles doped with Tm<sup>3+</sup>; Tm<sup>3+</sup>, Yb<sup>3+</sup> and Tm<sup>3+</sup>, Ho<sup>3+</sup> ions excited at 808 nm and (b) mechanism of generation of these emission bands. (c) Emission at ~1 μm generated by the Tm,Yb:KLu(WO<sub>4</sub>)<sub>2</sub> nanoparticles excited at 808 nm.

For  $\text{Tm}^{3+}$  doped and for  $\text{Tm}^{3+}$ ,  $\text{Yb}^{3+}$  co-doped nanoparticles the intensity of the 1.45  $\mu\text{m}$  band is almost insensitive to temperature changes, while the intensity of the 1.8  $\mu\text{m}$  band decreases as the temperature increased. Instead, for  $\text{Tm}^{3+}$ ,  $\text{Ho}^{3+}$  co-doped nanoparticles the intensity of the bands at 1.45 and 1.96  $\mu\text{m}$  decreases slightly with temperature, while the intensity of the 1.8  $\mu\text{m}$  band increases slightly as the temperature increases. This would indicate the existence of an energy backtransfer mechanism from  $\text{Ho}^{3+}$  to  $\text{Tm}^{3+}$ , as indicated in Figure 5(b), that is more efficient as the temperature increases. This gives an additional mechanism that can be used to determine the temperature by luminescence thermometry with these nanoparticles.

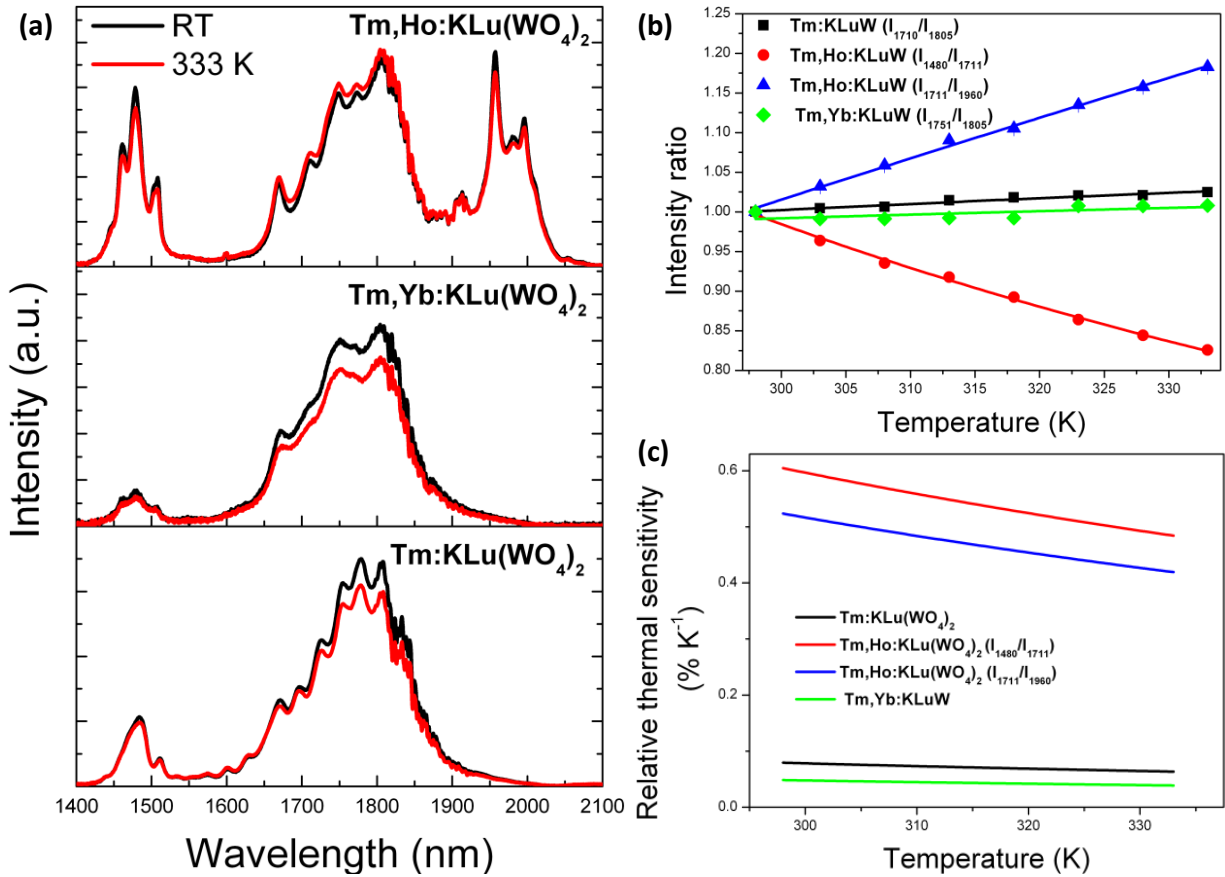


**Figure 6.** (a) Temperature dependence of the SWIR emissions for the KLu(WO<sub>4</sub>)<sub>2</sub> nanoparticles doped with Tm<sup>3+</sup>; Tm<sup>3+</sup>, Yb<sup>3+</sup> and Tm<sup>3+</sup>, Ho<sup>3+</sup> ions after pumping at 808 nm. (b) Intensity ratio between selected SWIR emission lines in Tm:KLu(WO<sub>4</sub>)<sub>2</sub>, Tm,Yb:KLu(WO<sub>4</sub>)<sub>2</sub> and Tm,Ho:KLu(WO<sub>4</sub>)<sub>2</sub> nanoparticles. (c) Relative thermal sensitivity of the intensity ratios considered in (b) as a function of temperature.

When we analyzed the intensity ratio between the bands located at 1.45 and 1.8  $\mu\text{m}$  after excitation at 808 nm we observed a lower slope for Tm:KLu(WO<sub>4</sub>)<sub>2</sub> nanoparticles when compared to that of Tm,Yb:KLu(WO<sub>4</sub>)<sub>2</sub> and Tm,Yb,Ho:KLu(WO<sub>4</sub>)<sub>2</sub> nanoparticles (see Figure S4) excited at 980 nm. However, when pumping at 808 nm we observed a linear evolution with a higher slope for the intensity ratio between the two peaks located

at 1710 and 1805 nm corresponding to two thermally coupled Stark sublevels of the  ${}^3F_4 \rightarrow {}^3H_6$  transition for the  $Tm^{3+}$ -doped nanoparticles. A maximum relative thermal sensitivity of 0.1 %  $K^{-1}$  for this FIR was calculated.

In the case of  $Tm,Yb:KLu(WO_4)_2$  nanoparticles, the intensity ratio, if we consider emission lines arising also from two Stark sublevels of the  ${}^3F_4 \rightarrow {}^3H_6$  transition, is almost constant with temperature, as can be seen in Figure 6(b), exhibiting also the smallest thermal sensitivity among the intensity ratios considered.

For the  $Tm^{3+}, Ho^{3+}$  co-doped nanoparticles we observed a linear dependence with a significant slope for the intensity ratio between the bands located at 1480 and 1780 nm and the bands located at 1780 and 1960 nm, respectively, as the temperature increased. The relative thermal sensitivity calculated in this case is a little higher than that obtained when excited at 980 nm, 0.61 %  $K^{-1}$  for the  $I_{1480}/I_{1780}$  and 0.52 %  $K^{-1}$  for the  $I_{1780}/I_{1960}$ , which would indicate a better performance for the  $Tm^{3+}, Ho^{3+}$  co-doped nanoparticles excited at 808 nm.

**3.4 Comparison of the performance of luminescence thermometers based on lanthanide-doped nanoparticles operating in different spectral ranges.** The comparison among relative thermal sensitivities for all the samples analyzed in this work and other ratiometric systems based on Ln-doped nanoparticles extracted from the literature in the spectral range from the visible to the SWIR is presented in Figure 7(a). In this graph, the spectral range in which the different nanoparticles can be used is also included.

As can be seen in Figure 7(a), the relative thermal sensitivity achieved by our nanoparticles in the SWIR region, especially those doped with  $Tm^{3+}$ , is higher than the

one achieved with most of the luminescent nanoparticles operating in the I- and II-BWs, defined as the spectral ranges from 650-950 nm (I-BW) and 1000-1350 nm (II-BW).<sup>11,12</sup> Their thermal sensitivities are only surpassed by that of Er,Yb:NaYF<sub>4</sub> nanoparticles operating in the visible,<sup>33</sup> Ho,Tm:KLu(WO<sub>4</sub>)<sub>2</sub><sup>31</sup> and Tm,Yb:GdVO<sub>4</sub>@SiO<sub>2</sub> core-shell nanoparticles<sup>48</sup> operating in the I-BW, Nd:NaGdF<sub>4</sub> + CdS/PbS/ZnS composite structures operating in the II-BW,<sup>18</sup> and NaGdF<sub>4</sub> core-shell nanoparticles doped with Er and Nd operating between the II-BW and the SWIR.<sup>49</sup> Thus, we consider that the emissions in the SWIR of these nanoparticles can be used as efficient luminescent nanothermometers.

Figure 7(b) presents the data reported in the literature for the penetration depth in biological tissues of the light generated by different luminescent materials along the different spectral regions. As can be seen, the penetration depth in the SWIR region is higher than the one that can be achieved in the other spectral regions, being only surpassed by that of  $\alpha$ -Tm:NaYF<sub>4</sub>@CaF<sub>2</sub> core-shell nanoparticles injected in pork meat operating in the I-BW due to their high quantum yield (~0.6 %).<sup>50</sup>

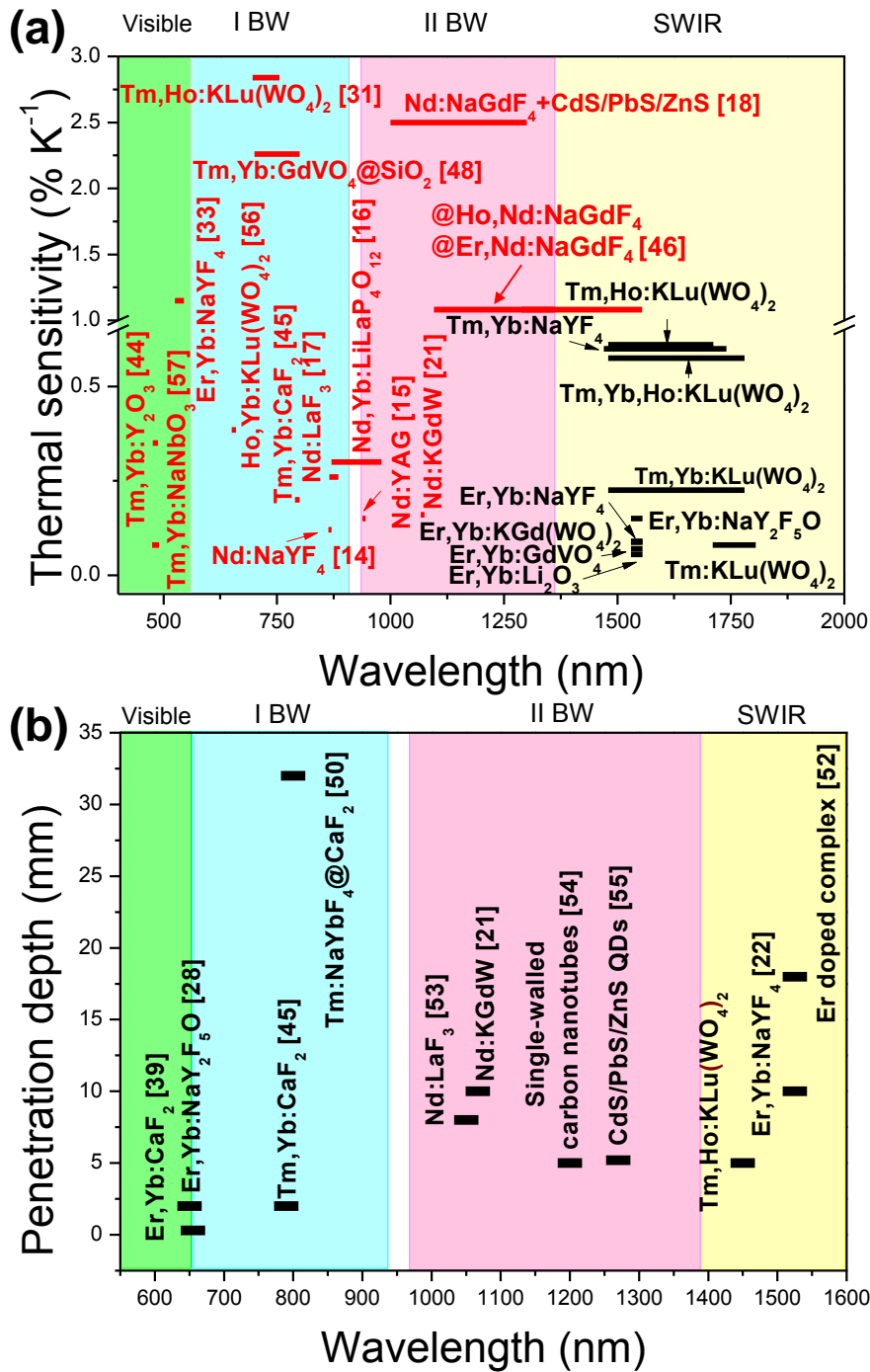


**Figure 7.** (a) Comparison of the relative thermal sensitivities of Ln-doped luminescent thermometers operating in the different spectral regions. (b) Penetration depth in

biological tissues reported for luminescent systems operating in the different spectral regions.

**3.5 *Ex-vivo* luminescence thermometry in the SWIR.** In order to prove the potentiality of these nanoparticles for temperature sensing purposes in biological tissues, we performed an *ex-vivo* temperature sensing experiment using chicken breast, since it shows optical characteristics comparable to those of human tissues.<sup>51</sup> The 1480 and 1711 nm emissions generated by Tm,Ho:KLu(WO<sub>4</sub>)<sub>2</sub> nanoparticles were chosen for this experiment as their intensity ratio showed the highest thermal sensitivity when pumped at 808 nm.

For this, Tm,Ho:KLu(WO<sub>4</sub>)<sub>2</sub> nanoparticles were deposited on a microscope glass slide on top of which a slice of chicken breast ~2 mm thick was placed. This thickness was limited by the optical setup we used in the experiment. A heating gun, with a fixed power of 1 W and fixed to a horizontal moving stage to control its movement, was used to induce the heating of the chicken breast. The heating gun was moved away from its initial position, close to the chicken breast sample, to generate a decrease of temperature in the biological tissue. Also, the maximum temperature reached in the chicken breast was controlled not to overpass 318 K (45 °C) to avoid its denaturalization. A fiber-coupled diode laser with emission at 808 nm and a power of 200 mW was focused on the nanoparticles by means of a microscope objective with 40X magnification and N. A. = 0.6. The emission arising from the nanoparticles through the chicken breast was collected by the same objective, and after passing a dichroic filter for elimination of the excitation wavelength, was sent to the Yokogawa AQ6375 OSA to record the spectra.

Prior to this experiment, we undertook a control experiment to confirm the negligible heating effect of the 808 nm radiation by exciting the nanoparticles around 10 min inside the chicken breast, while the heating gun was off. We can confirm that the heating effect observed in our experiment arose only from the effect of the hot air generated by the heating gun.

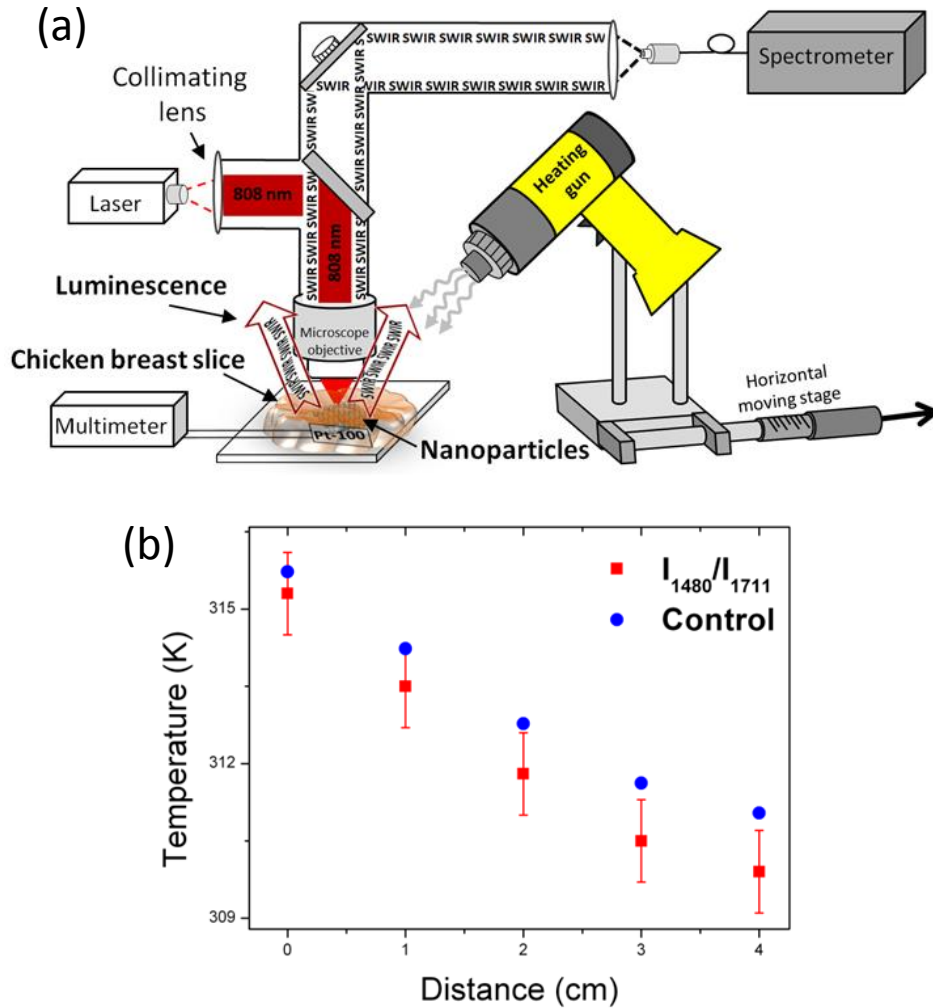


**Figure 8.** (a) Scheme of the setup used in the temperature sensing experiment inside the chicken breast. (b) Temperature data recorded by luminescent nanoparticles and thermocouple (control) during the heating process.

After the analysis of the emission spectra, and comparing the obtained data with the calibration curve in Figure 6(b), the temperature was deduced. Moreover, in order to verify the data, temperature was also recorded by a digital multimeter connected to a small Pt-100 thermocouple located inside the chicken breast slide, very close to the nanoparticles. The scheme of the setup is shown in Figure 8(a).

The temperature profile of the heating process determined from the emission of the luminescent nanoparticles and the Pt-100 thermo-resistor are shown in Figure 8(b). It can be observed that by moving away the heating gun from the chicken sample, a temperature drop of  $\sim 1.5 \text{ K cm}^{-1}$  was generated. The temperature dropping could be monitored both with the Pt-100 thermocouple and the intensity ratio determined from the intensity of the 1480 and 1711 nm emission lines of Ho,Tm:KLu(WO<sub>4</sub>)<sub>2</sub> nanoparticles. The intensity ratio showed a difference of 0.8 K to respect the thermocouple that might be due to the different thermal conductivity of the two materials (nanoparticles and thermocouple), or also to the different location of the thermal probes (the thermocouple was located in the chicken breast, while the luminescent nanoparticles were located below it). The experiment demonstrates the potentiality of using luminescent nanoparticles generating SWIR emission lines for temperature determination purposes in biomedical applications with a thermal resolution around  $\pm 0.5 \text{ K}$ , below the value predicted theoretically for particles operating in this spectral region.<sup>49</sup>

***Ex-vivo* SWIR imaging experiment.** These emissions in the SWIR can also be used for bioimaging applications. An scheme of the setup used for this purpose in a chicken breast sample is shown in Figure 9(a). In this case, a drop of the dispersion of the Ho,Tm:KLu(WO<sub>4</sub>)<sub>2</sub> nanoparticles in water, with a concentration of  $0.5 \text{ mg ml}^{-1}$ , was

placed between two microscope slides, and a piece of chicken breast with a thickness of 0.5 cm was placed over them. A cw diode laser emitting at 808 nm with a power of 7.5 W, located 5 cm away from the sample, and producing a spot of  $\sim 3.5$  cm on it, which generated an excitation density of  $0.78 \text{ W cm}^{-2}$ , was used for exciting the luminescent nanoparticles. The signal was collected by a Peltier cooled InGaAs IR Xenics camera with an attached filters wheel that allowed collecting the emission arising from particular wavelength ranges of interest and eliminate the excitation laser.

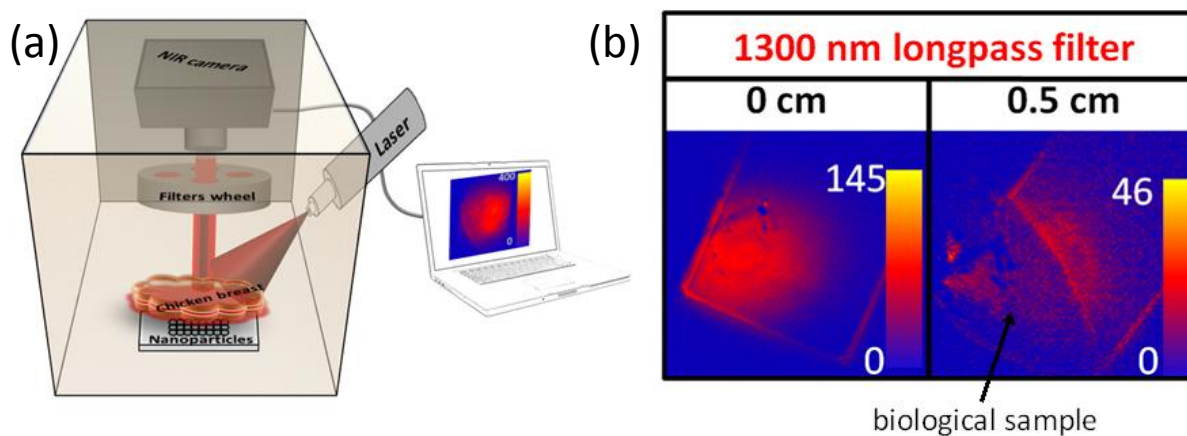


**Figure 9.** (a) Scheme of the setup used for the *ex-vivo* SWIR imaging experiment. (b) SWIR images achieved using the light emitted by the  $\text{Ho,Tm:KLu(WO}_4)_2$  nanoparticles covered or not with a piece of chicken breast 0.5 cm thick.

Figure 9(b) shows the images recorded in the SWIR range. As can be seen, the signal recorded using a 1300 nm longpass filter allows identifying the shape of the chicken breast sample. This image would correspond only to the  $\sim 1.45 \mu\text{m}$  emission arising from the  $\text{Ho,Tm:KLu(WO}_4)_2$  nanoparticles, since the spectral sensitivity of the InGaAs detector does not go beyond  $1.7 \mu\text{m}$ . Thus, we believe that with a detector that allows detecting beyond this limit, the bioimaging in the SWIR region could still be improved. What is also important to note is that this image corresponds to the emission generated

0.5 cm below the surface of the chicken sample, thus indicating that at least a penetration depth of 0.5 cm can be achieved using these nanoparticles.

#### 4. CONCLUSION

In summary, we analyzed the SWIR emissions of  $\text{Er}^{3+}$ ,  $\text{Tm}^{3+}$  and  $\text{Ho}^{3+}$  in different hosts and their potentiality for luminescence thermometry in this spectral region.

The 1.55  $\mu\text{m}$  emission band generated by  $\text{Er}^{3+}$  has different thermally couple Stark sub-levels that can be used for temperature sensing purposes, especially in telecommunication systems, despite having a relatively low thermal sensistivity.

In the case of  $\text{Tm}^{3+}$ -doped nanoparticles, the emissions arising from the  ${}^3\text{F}_4$  and  ${}^3\text{H}_4$  energy levels, that are electronically coupled, can be used for luminescence thermometry purposes with a higher thermal sensitivity when compared to  $\text{Er}^{3+}$ -doped systems.

Adding  $\text{Ho}^{3+}$  to the system generate an efficient energy transfer between  $\text{Tm}^{3+}$  and  $\text{Ho}^{3+}$ , resulting in a new emission line centered at 1.96  $\mu\text{m}$  that can also be used for luminescence thermometry purposes. The excitation of these nanoparticles at 808 nm increases their thermal sensitivity to values comparable to those reported previously in the visible and higher than those reported in the BWs, avoiding at the same time the undesired heating effects of pumping at 980 nm.

Furthermore, we demonstrated not only the potentiality of SWIR emissions for luminescence thermometry but also for bioimaging in *ex-vivo* experiments by monitoring the heat generated by hot air in chicken meat, with a thermal resolution  $\sim 0.5$  K and a penetration depth of at least 0.5 cm.

We believe that the results presented here will be useful for the application of luminescence thermometry to some specific biological tissues, like those containing melanine, that have not been considered yet in this field.

## ASSOCIATED CONTENT

### **Supporting information**

## AUTHOR INFORMATION

### **Corresponding Author**

\*Email: joan josep.carvajal@urv.cat

### **Notes**

The authors declare no competing financial interest.

## ACKNOWLEDGMENT

This work was supported by the Spanish Government under Projects No. TEC2014-55948-R and MAT2016-75716-C2-1-R (AEI/FEDER, UE), and by Generalitat de Catalunya under Project No. 2017SGR755. Ol. A. Savchuk was supported by Catalan Government through the fellowship 2015FI\_B2 00136. P.H.G. thanks the ministerio de Economía y Competitividad for Juan de la Cierva program (JCI-2012-12885).

## REFERENCES

- (1) R.B. Roemer, *Annu. Rev. Biomed. Eng.* 1 (1989) 347-376.
- (2) A.Y. Cheung, A. Neyzari, *Cancer Res.* 44 (1984) 4736-4744.
- (3) N.P. O'Grady, P.S. Barie, J.G. Bartlett, T. Bleck, G. Garvey, J. Jacobi, P Linden, D.G. Maki, M. Nam, W. Pasculle, *Clin. Infect. Dis.* 26 (1998) 1042-1059.
- (4) M. Miyakawa, J.C. Bolomey, *Non invasive Thermometry of a Human Body*, CRC press, New York, 1995.
- (5) C.D.S. Brites, P.P. Lima, N.J.O. Silva, A. Millán, V.S. Amaral, F. Palacio, L.D. Carlos, *Nanoscale* 4 (2012) 4799-4829.
- (6) D. Jaque, F. Vetrone, *Nanoscale* 4 (2012) 4301-4326.
- (7) M. Haase, H. Schäfer, *Angew. Chem. Int. Ed.* 50 (2011) 5808-5829.
- (8) M.L. Debasu, D. Ananias, I. Pastoriza-Santos, L.M. Liz-Marzán, J. Rocha, L.D. Carlos, *Adv. Mater.* 25 (2013) 4868-4874.
- (9) F. Vetrone, R. Naccache, A. Zamarron, A.J. de la Fuente, F. Sanz-Rodríguez, L.M. Maestro, E.M. Rodriguez, D. Jaque, J. García Sole, J.A. Capobianco, *ACS Nano* 4 (2010) 3254-3258.
- (10) S.P. Wang, S. Westcott, W. Chen, *J. Phys. Chem. B* 106 (2002) 11203-11209.
- (11) L.A. Sordillo, Y. Pu, S. Pratavieira, Y. Budansky, and R.R. Alfano, *J. Biomed. Opt.* 19 (2014) 056004.
- (12) R.A. Weissleder, *Nat. Biotechnol.* 19 (2001) 316-317.
- (13) E. Carrasco, B. del Rosal, F. Sanz-Rodríguez, A. Juarranz de la Fuente, P. Haro-Gonzalez, U. Rocha, K.U. Kumar, C. Jacinto, J.G. Sole, D. Jaque, *Adv. Func. Mater.* 25 (2015) 615-626.

- (14) D. Wawrzynczyk, A. Bednarkiewicz, M. Nyk, W. Streck, M. Samoc, *Nanoscale* 4 (2012) 6959-6961.
- (15) A. Benayas, B. del Rosal, A. Perez-Delgado, K. Santacruz-Gomez, D. Jaque, G.A. Hirata, F. Vetrone, *Adv. Opt. Mater.* 3 (2015) 687-694.
- (16) L. Marciniak, A. Bednarkiewicz, M. Stefanski, R. Tomala, D. Hreniak, W. Streck, *Phys. Chem. Chem. Phys.* 17 (2015) 24315-24321.
- (17) U. Rocha, C.J. da Silva, W.F. Silva, I. Guedes, A. Benayas, L.M. Maestro, M.A. Elias, E. Bovero, F.C.J.M. van Veggel, J.A.G. Sole, D. Jaque, *ACS Nano* 7 (2013) 1188-1199.
- (18) E.N. Ceron, D.H. Ortgies, B. del Rosal, F. Ren, A. Benayas, F. Vetrone, D. Ma, F. Sanz-Rodriguez, J.G. Sole, D. Jaque, E.M. Rodriguez, *Adv. Mater.* 27 (2015) 4781-4787.
- (19) I. Villa, A. Vedda, I.X. Cantarelli, M. Pedroni, F. Piccinelli, M. Bettinelli, A. Speghini, M. Quintanilla, F. Vetrone, U. Rocha, C. Jacinto, E. Carrasco, F.S. Rodríguez, A. Juarranz, B. del Rosal, D.H. Ortgies, P.H. Gonzalez, J.G. Sole, D. Jaque, *Nano Res.* 8 (2015) 649-665.
- (20) X. Mateos, M.C. Pujol, F. Güell, M. Galan, R.M. Sole, J. Gavalda, M. Aguiló, J. Massons, F. Diaz, *IEEE J. Quant. Electron.* 40 (2004) 759-770.
- (21) O.I. Savchuk, J.J. Carvajal, L.G. de la Cruz, P. Haro-Gonzalez, M. Aguiló, F. Diaz, *J. Mater. Chem. C* 4 (2016) 7397-7405.
- (22) D.J. Naczynski, M.C. Tan, M. Zevon, B. Wall, J. Kohl, A. Kulesa, S. Chen, C.M. Roth, R.E. Riman, P.V. Moghe, *Nat. Commun.* 4 (2013) 2199-2219.

- (23) S. Diao, G. Hong, A.L. Antaris, J.L. Blackburn, K. Cheng, Z. Cheng, H. Dai, *Nano Res.* 8 (2015) 3027-3034.
- (24) I. Villa, A. Vedda, I.X. Cantarelli, M. Pedroni, F. Piccinelli, M. Bettinelli, A. Speghini, M. Quintanilla, F. Vetrone, U. Rocha, C. Jacinto, E. Carrasco, F.S. Rodriguez, A. Juarranz, B. del Rosal, D.H. Ortgies, P.H. Gonzalez, J. García Solé, D. Jaque, *Nano Res.* 8 (2015) 649-665.
- (25) V.D. Rodriguez, V.K. Tikhomirov, J. Mendez-Ramos, J. del-Castillo, C. Gorller-Walrand, *J. Nanosci. Nanotechnol.* 9 (2009) 2072
- (26) V.K. Tikhomirov, M. Mortier, P. Gredin, G. Patriarche, C. Gorller-Walrand, V.V. Moshchalkov, *Opt. Express* 16 (2008) 14544
- (27) M. Mortier, G. Patriarche, *Opt. Mater.* 28 (2006) 1401
- (28) Ol.A. Savchuk, P. Haro-Gonzalez, J.J. Carvajal, D. Jaque, J. Massons, M. Aguiló, F. Diaz, *Nanoscale* 6 (2014) 9727-9733.
- (29) Ol.A. Savchuk, J.J. Carvajal, M.C. Pujol, J. Massons, P. Haro-González, O. Martínez, J. Jiménez, M. Aguiló, F. Díaz, *J. Lumin.* 169 (2016) 711-716.
- (30) M. Galceran, M.C. Pujol, P. Gluchowski, W. Strek, J.J. Carvajal, X. Mateos, M. Aguiló, F. Díaz, *J. Am. Ceram. Soc.* 93 (2010) 3764-3772.
- (31) Ol.A. Savchuk, J.J. Carvajal, C.D.S. Brites, L.D. Carlos, M. Aguiló, F. Diaz, *Nanoscale* (submitted)
- (32) O.A. Savchuk, J.J. Carvajal, M.C. Pujol, E.W. Barrera, J. Massons, M. Aguiló, F. Diaz, *J. Phys. Chem. C* 119 (2015) 18546-18558.
- (33) E. Hemmer, M. Quintanilla, F. Legare, F. Vetrone, *Chem. Mater.* 27 (2015) 235-244.

- (34) L.H. Fischer, G.S. Harms, O.S. Wolbeis, *Angew. Chem. Int. Ed.* 50 (2011) 4546-4551.
- (35) S.A. Wade, S.F. Collins, G.W. Baxter, *J. Appl. Phys.* 94 (2003) 4743-4756.
- (36) C.H. Huang, L. McCaughan, *IEEE J. Sel. Top. Quant. Electron.* 2 (1996) 367-372.
- (37) J.D.B. Bradley, M. Pollnau, *Laser Photon. Rev.* 5 (2011) 368-403.
- (38) L. Tao, Y.H. Tsang, B. Zhou, B. Richards, A. Jha, *J. Non-Cryst. Solids* 358 (2012) 1644-1648.
- (39) M. Faleonieri, A. Lanzi, G. Salvetti, *Appl. Phys. B* 62 (1996) 537-546.
- (40) H. Hayashi, S. Tanabe, T. Hanada, *J. Appl. Phys.*, 89 (2001) 1041-1045.
- (41) E.J. McLaurin, L.R. Bradshaw, D.R. Gamelin, *Chem. Mater.* 25 (2013) 1283-1292.
- (42) Ol.A. Savchuk, J.J. Carvajal, C. Cascales, J. Massons, M. Aguiló, F. Díaz, *J. Mat. Chem. C* 4 (2016) 6602-6613.
- (43) A. Brenier, J. Rubin, R. Moncorge, C. Pedrini, *J. Phys.* 50 (1989) 1463-1482.
- (44) D. Li, Y. Wang, X. Zhang, K. Yang, L. Liu, Y. Song, *Opt. Commun.* 285 (2012) 1925-1928.
- (45) N.N. Dong, M. Pedroni, F. Piccinelli, G. Conti, A. Sbarbati, J.E. Ramírez-Hernández, L.M. Maestro, M.C. Iglesias-de la Cruz, F. Sanz-Rodriguez, A. Juarranz, F. Chen, F. Vetrone, J.A. Capobianco, J.G. Sole, M. Bettinelli, D. Jaque, A. Speghini, *ACS Nano* 5 (2011) 8665-8671.
- (46) W. Xu, X.Y. Gao, L.J. Zheng, Z.G. Zhang, W.W. Cao, *Sens. Actuat. B* 173 (2012) 250.
- (47) L. Xing, Y. Xu, R. Wang, W. Xu, Z. Zhang, *Opt. Lett.* 39 (2014) 454-456

- (48) Ol.A. Savchuk, J.J. Carvajal, C. Cascales, P. Haro-Gonzalez, F. Sanz-Rodriguez, M. Aguilo, F. Diaz, *Nanotechnology* (submitted).
- (49) A. Skripka, A. Benayas, R. Marin, P. Canton, E. Hemmer, F. Vetrone, *Nanoscale* 9 (2017) 3079-3085.
- (50) G. Chen, J. Shen, T.Y. Ohulchanskyy, N.J. Patel, A. Kutikov, Z. Li, J. Song, R.K. Pandey, H. Agren, P.N. Prasad, G. Han, *ACS Nano* 6 (2012) 8280-8287.
- (51) G. Marquez, L.V. Wang, S.P. Lin, J.A. Schwartz, S.L. Thomsen, *Appl. Opt.* 37 (1998) 798-804.
- (52) R. Wang, X. Li, L. Zhou, F. Zhang, *Angew. Chem.* 126 (2014) 12282-12286.
- (53) U. Rocha, K.U. Kumar, C. Jacinto, I. Villa, F. Sanz-Rodriguez, M.C. de la Cruz, A. Juarranz, E. Carrasco, F.C.J.M. van Veggel, E. Bovero, J.G. Sole, D. Jaque, *Small* 10 (2014) 1141-1154.
- (54) K. Welsher, S.P. Sherlock, H. Dai, *PNAS* 108 (2011) 8943-8948.
- (55) A. Benayas, F. Ren, E. Carrasco, V. Marzal, B. del Rosal, B.A. Gonfa, A. Juarranz, F. Sanz-Rodriguez, D. Jaque, J. Garcia-Sole, D. Ma, F. Vetrone, *Adv. Func. Mater.* 25 (2015) 6650-6659.
- (56) O.A. Savchuk, J.J. Carvajal, M.C. Pujol, E.W. Barrera, J. Massons, M. Aguilo, F. Diaz, *J. Phys. Chem. C* 119 (2015) 18546-18558.
- (57) A.F. Pereira, U.K. Kumar, W.F. Silva, W.Q. Santos, D. Jaque, C. Jacinto, *Sens. Actuat. B* 213 (2015) 65-71.